



**HAL**  
open science

# Super-resolution reconstruction of brain 3D magnetic resonance images using a coupled tensor multilinear approximation

Clémence Prévost, F Odille

► **To cite this version:**

Clémence Prévost, F Odille. Super-resolution reconstruction of brain 3D magnetic resonance images using a coupled tensor multilinear approximation. 2022. hal-03687137

**HAL Id: hal-03687137**

**<https://hal.science/hal-03687137v1>**

Preprint submitted on 3 Jun 2022

**HAL** is a multi-disciplinary open access archive for the deposit and dissemination of scientific research documents, whether they are published or not. The documents may come from teaching and research institutions in France or abroad, or from public or private research centers.

L'archive ouverte pluridisciplinaire **HAL**, est destinée au dépôt et à la diffusion de documents scientifiques de niveau recherche, publiés ou non, émanant des établissements d'enseignement et de recherche français ou étrangers, des laboratoires publics ou privés.

# Super-resolution reconstruction of brain 3D magnetic resonance images using a coupled tensor multilinear approximation

C. Prévost<sup>1</sup>, F. Odille<sup>2,3</sup>,

**Abstract**—In this paper, we address the multi-frame super-resolution MRI problem. We formulate the reconstruction problem as a coupled tensor multilinear approximation. We prove that exact recovery of the high-resolution 3D isotropic image is achievable for a variety of multilinear ranks. We propose a simple algorithm based on Tikhonov regularization to perform the reconstruction. Our simulations on real datasets illustrates the good performance of the proposed approach, with a lower computation time than state-of-the-art methods.

## I. INTRODUCTION

Magnetic resonance imaging (MRI) is a versatile medical imaging modality, providing excellent contrast between soft tissues. The acquisition parameters can indeed be tuned in order to make this contrast sensitive to various tissue properties, such as proton density, and longitudinal and transverse relaxation times (respectively  $T_1$  and  $T_2$ ). MRI acquisition consists of repeatedly exciting protons in the human body, using various electromagnetic pulses, and acquiring a small amount of Fourier samples from the image.

The observations in the frequency domain are then recast into the spatial domain by an inverse Fourier transform operation. Typical MRI data consist in 2D or 3D images in arbitrary orientations. The latter possess two in-plane spatial dimensions and a third spatial dimension in the slice direction, hence they can be seen as tensors.

However, MRI suffers from a relatively slow acquisition time, typically on the order of minutes. This technical limitation can prevent the acquisition of 3D high-resolution images to be possible or optimal. To circumvent this drawback, super-resolution techniques have been shown to be efficient in a number of situations [1], [2], [3]. They consist in recovering a 3D high-resolution image from one or several low-resolution observations.

Recently, it been proposed to recover the high-resolution image from a single low-resolution observation using deep learning [4], [5]. However, in the presence of small lesions, it may be preferable to consider several observations for diagnostic use of the images. The observations can be incorporated into a fusion model, thus providing additional information compared to separate processing [6]. Using the fusion paradigm avoids to rely on an external patient database for the prior. Therefore, in the remainder, we will focus on the problem of super-resolution reconstruction from multiple observations, also termed multi-frame super-resolution.

Multi-frame super-resolution MRI consists of acquiring several complementary observations of the organ of interest, e.g. three orthogonal scans [7], or three scans with sub-voxel shifts in the slice direction [8]. Each observation has high in-plane resolutions (1 mm or less) in the first two dimensions, and low resolution in the slice direction (typically 3 to 10 mm). The acquisition process can be modelled, including a blurring/downsampling operator in the slice direction. Patient motion (bulk head motion, breathing motion, heart beating etc.) can also be taken into account, but this is generally performed as a pre-processing step, before super-resolution reconstruction, using motion-compensated reconstruction (in case of intra-scan motion, i.e. to resolve motion blurring) [9] and/or image registration (in case of inter-scan motion, i.e. to resolve misalignment from scan to scan)[10].

The super-resolution problem is most often solved by regularized inversion. Besides the classic Tikhonov regularization [11], total variation [12] or Beltrami energy regularizers [9] have been proposed, as well as constraints on the rank of the matricized image<sup>1</sup> [13], and patch-based regularization methods [14]. The last two methods are intended to exploit the low-rank structure of the images. Iterative solvers are used in all these cases, such as the conjugate gradient (Tikhonov), primal dual gradient descent (Beltrami) or the alternating direction method of multipliers (low-rank and patch-based methods).

However, matrix patch-based methods possess a high computational burden, as they require many operations for extracting patches from the image, sorting them, and performing dimensionality reduction. They also fail at preserving the natural tensor shape of the observations. More importantly, no theoretical guarantees for exact reconstruction of the high-resolution images were provided.

Tensor-based reconstruction methods were recently envisioned in some engineering fields such as remote sensing of spectrum cartography [15], [16], [17]. In the field of medical imaging, coupled tensor models were used for the reconstruction of dynamic cardiac images [18] of functional MRI reconstruction [19], for instance. Such approaches preserved the structural information between the dimensions of the images. Theoretical guarantees for exact image recovery could be formulated under mild rank conditions, see for instance [15], [16].

Several low-rank factorizations can be considered for approximating tensor data. The multilinear (also known as Tucker) factorization was considered in [16] with remote sensing applications. The reconstruction problem was formulated

<sup>1</sup>Univ. Lille, CNRS, Centrale Lille, UMR 9189 CRISTAL, Lille, France; <sup>2</sup>Inserm, Université de Lorraine, U1254 IADI, Nancy, France; <sup>3</sup>Inserm, Université de Lorraine, CHRU Nancy, CIC-IT 1433, Nancy, France

<sup>1</sup>This method was applied to single-frame super-resolution.

as a coupled Tucker approximation. A closed-form SVD-based algorithm was proposed. The approach of [16] considered 3D image reconstruction from two degraded tensors. Each observation had two degraded dimensions, which made the recovery conditions in [16] less flexible than the ones proposed in this paper.

In this paper, we propose a novel tensor-based approach for multi-frame super-resolution MRI. The proposed approach is based on a coupled low-rank multilinear approximation of three 3D observations in image space. We introduce a simple closed-form algorithm with low computational burden, named isometRic Image Reconstruction by COupled Tensor Tucker Approximation (RICOTTA), that is inspired by the higher-order SVD [21]. We prove that our approach achieves exact reconstruction of the high-resolution 3D image for a variety of multilinear ranks. We illustrate the performance of our method on a set of synthetic and real datasets. We show that our algorithm yields good reconstruction, with lower computation time than matrix-based super-resolution methods.

This paper is organized as follows. The remaining of Section I introduces the main notations and tensor definitions. Section II contains the low-rank tensor model and the proposed algorithm. In Section III, we provide generic conditions for exact recovery of the HR II in the noiseless case. Finally, Section IV contains the numerical experiments.

#### A. Basic notation

In this paper we mainly follow [22] in what concerns the tensor notation (see also [23]). The following fonts are used: lowercase ( $a$ ) or uppercase ( $A$ ) plain font for scalars, boldface lowercase ( $\mathbf{a}$ ) for vectors, uppercase boldface ( $\mathbf{A}$ ) for matrices, and calligraphic ( $\mathcal{A}$ ) for  $N$ -D arrays (tensors). Vectors are, by convention, one-column matrices. The elements of vectors/matrices/tensors are accessed as  $a_i$ ,  $A_{i,j}$  and  $\mathcal{A}_{i_1, \dots, i_N}$  respectively.  $\mathbb{R}$  stands for the real line.

For a matrix  $\mathbf{A}$ , we denote its transpose and Moore-Penrose pseudoinverse as  $\mathbf{A}^\top$  and  $\mathbf{A}^\dagger$  respectively. The notation  $\mathbf{I}_M$  is used for the  $M \times M$  identity matrix and  $\mathbf{0}_{L \times K}$  for the  $L \times K$  matrix of zeroes. We use the symbol  $\boxtimes$  for the Kronecker product of matrices (in order to distinguish it from the tensor product  $\otimes$ ), and  $\odot$  for the Khatri-Rao product.

For a matrix  $\mathbf{X} \in \mathbb{R}^{m \times n}$ , we denote by  $\sigma_{max}(\mathbf{X})$  and  $\sigma_{min}(\mathbf{X})$  the largest and the smallest of the  $\min(m, n)$  singular values of  $\mathbf{X}$ . We also denote by  $\text{tSVD}_R(\mathbf{X}) \in \mathbb{R}^{n \times R}$  a matrix containing  $R$  leading right singular vectors of  $\mathbf{X}$ .

We use  $\text{vec}\{\cdot\}$  for the standard column-major vectorization of a tensor or a matrix. Operator  $\bullet_p$  denotes contraction on the  $p$ th index of a tensor; when contracted with a matrix, summation is always performed on the second index of the matrix, e.g.,  $[\mathcal{A} \bullet_1 \mathbf{M}]_{ijk} = \sum_\ell \mathcal{A}_{\ell jk} M_{i\ell}$ . For a tensor  $\mathcal{Y} \in \mathbb{R}^{I \times J \times K}$ , its first unfolding is denoted by  $\mathbf{Y}^{(1)} \in \mathbb{R}^{JK \times I}$ .

#### B. Tensor decompositions

For a tensor  $\mathcal{G} \in \mathbb{R}^{R_1 \times R_2 \times R_3}$  and matrices  $\mathbf{U} \in \mathbb{R}^{I \times R_1}$ ,  $\mathbf{V} \in \mathbb{R}^{J \times R_2}$  and  $\mathbf{W} \in \mathbb{R}^{K \times R_3}$ , the following shorthand notation is used for the multilinear product:

$$[\mathcal{G}; \mathbf{U}, \mathbf{V}, \mathbf{W}] = \mathcal{G} \bullet_1 \mathbf{U} \bullet_2 \mathbf{V} \bullet_3 \mathbf{W}. \quad (1)$$

which means that the  $(i, j, k)$ th entry of the above array is

$$\sum_{pqr} G_{pqr} U_{ip} V_{jq} W_{kr}.$$

If  $\mathcal{Y} = [\mathcal{G}; \mathbf{U}, \mathbf{V}, \mathbf{W}]$ , the following identities hold for its vectorization and unfoldings, respectively:

$$\begin{aligned} \text{vec}\{\mathcal{Y}\} &= (\mathbf{W} \boxtimes \mathbf{V} \boxtimes \mathbf{U}) \text{vec}\{\mathcal{G}\}, \\ \mathbf{Y}^{(1)} &= (\mathbf{W} \boxtimes \mathbf{V}) \mathbf{G}^{(1)} \mathbf{U}^\top. \end{aligned}$$

If, in addition,

$$R_1 = \text{rank}(\mathbf{Y}^{(1)}), R_2 = \text{rank}(\mathbf{Y}^{(2)}), R_3 = \text{rank}(\mathbf{Y}^{(3)}),$$

then the multilinear product is called Tucker decomposition of  $\mathcal{Y}$  and  $(R_1, R_2, R_3)$  are called the multilinear ranks.

## II. SUPER-RESOLUTION BY COUPLED MULTILINEAR APPROXIMATION

### A. The image reconstruction problem

We aim at recovering a high-resolution 3D isotropic image (HR II) with high resolutions. This image can be viewed as a 3-dimensional tensor  $\mathcal{Z} \in \mathbb{R}^{I \times J \times K}$ , where  $K$  represents the number of frontal slices and  $I$  and  $J$  stand for the spatial resolutions of each slice.

We have three low-resolution 3D images (LRI) available, that can be viewed as degraded versions of  $\mathcal{Z}$  in one given dimension. The observations are denoted to as  $\mathcal{Y}_1 \in \mathbb{R}^{I_1 \times J \times K}$ ,  $\mathcal{Y}_2 \in \mathbb{R}^{I \times J_2 \times K}$  and  $\mathcal{Y}_3 \in \mathbb{R}^{I \times J \times K_3}$ , respectively. The dimensions  $I_1$ ,  $J_2$  and  $K_3$  stand for the degraded dimensions, i.e.,  $I_1 \ll I$ ,  $J_2 \ll J$  and  $K_3 \ll K$ , respectively. The ratio of degraded to high-resolution dimensions depend on the machine settings and acquisition sequence. Formally, we can express the degradation model as mode product of the HR II  $\mathcal{Z}$  with some degradation matrices as

$$\begin{cases} \mathcal{Y}_1 &= \mathcal{Z} \bullet_1 \mathbf{D}_1 + \mathcal{E}_1, \\ \mathcal{Y}_2 &= \mathcal{Z} \bullet_2 \mathbf{D}_2 + \mathcal{E}_2, \\ \mathcal{Y}_3 &= \mathcal{Z} \bullet_3 \mathbf{D}_3 + \mathcal{E}_3. \end{cases} \quad (2)$$

The degradation matrices  $\mathbf{D}_i$  ( $i = 1, 2, 3$ ) are known down-sampling matrices such as  $\mathbf{D}_1 \in \mathbb{R}^{I_1 \times I}$ ,  $\mathbf{D}_2 \in \mathbb{R}^{J_2 \times J}$  and  $\mathbf{D}_3 \in \mathbb{R}^{K_3 \times K}$  and depend on the sensor specificities. The tensors  $\mathcal{E}_i$  ( $i = 1, 2, 3$ ) represent white Gaussian noise terms.

The image reconstruction problem can thus be expressed as the following optimization problem

$$\begin{aligned} \min_{\hat{\mathcal{Z}}} & \lambda_1 \|\mathcal{Y}_1 - \hat{\mathcal{Z}} \bullet_1 \mathbf{D}_1\|_F^2 + \lambda_2 \|\mathcal{Y}_2 - \hat{\mathcal{Z}} \bullet_2 \mathbf{D}_2\|_F^2 \\ & + \lambda_3 \|\mathcal{Y}_3 - \hat{\mathcal{Z}} \bullet_3 \mathbf{D}_3\|_F^2 + \mu \mathcal{R}(\hat{\mathcal{Z}}), \end{aligned} \quad (3)$$

where the scalars  $\lambda_i$  ( $i = 1, 2, 3$ ) are balance parameters that control the weights of the LRI in the cost function. The operator  $\mathcal{R}(\cdot)$  is a regularization operator and performs Tikhonov regularization [24] on the reconstructed HR II  $\hat{\mathcal{Z}}$ . Its weight is controlled by the user-specified scalar  $\mu$ . Including the regularization term in the cost function promotes smoothness of the image in the spatial dimensions, while preserving the details and reducing the impacts of artifacts that may occur by performing low-rank approximation.

### B. Coupled Tucker reformulation

In this paper, we propose to use a coupled tensor multilinear (Tucker) approximation to solve the reconstruction problem (3). We assume that the HR II  $\mathcal{Z}$  admits a Tucker decomposition with low multilinear ranks  $(R_1, R_2, R_3)$  as

$$\mathcal{Z} = [\mathcal{G}; \mathbf{U}, \mathbf{V}, \mathbf{W}], \quad (4)$$

where  $\mathbf{U} \in \mathbb{R}^{I \times R_1}$ ,  $\mathbf{V} \in \mathbb{R}^{J \times R_2}$  and  $\mathbf{W} \in \mathbb{R}^{K \times R_3}$  are the factor matrices and  $\mathcal{G} \in \mathbb{R}^{R_1 \times R_2 \times R_3}$  is the core tensor.

Under this assumption, the degradation model (2) becomes

$$\begin{cases} \mathcal{Y}_1 &= [\mathcal{G}; \mathbf{D}_1 \mathbf{U}, \mathbf{V}, \mathbf{W}] + \mathcal{E}_1, \\ \mathcal{Y}_2 &= [\mathcal{G}; \mathbf{U}, \mathbf{D}_2 \mathbf{V}, \mathbf{W}] + \mathcal{E}_2, \\ \mathcal{Y}_3 &= [\mathcal{G}; \mathbf{U}, \mathbf{V}, \mathbf{D}_3 \mathbf{W}] + \mathcal{E}_3. \end{cases} \quad (5)$$

Furthermore, by plugging (5) in (3), solving the super-resolution problem can be viewed as minimizing a cost function  $f_T(\hat{\mathcal{G}}, \hat{\mathbf{U}}, \hat{\mathbf{V}}, \hat{\mathbf{W}})$  with respect to the low-rank factors  $\mathbf{U}$ ,  $\mathbf{V}$ ,  $\mathbf{W}$ ,  $\mathcal{G}$ . This cost function is such that

$$\begin{aligned} f_T(\hat{\mathcal{G}}, \hat{\mathbf{U}}, \hat{\mathbf{V}}, \hat{\mathbf{W}}) &= \lambda_1 \|\mathcal{Y}_1 - [\hat{\mathcal{G}}; \mathbf{D}_1 \hat{\mathbf{U}}, \hat{\mathbf{V}}, \hat{\mathbf{W}}]\|_F^2 \\ &+ \lambda_2 \|\mathcal{Y}_2 - [\hat{\mathcal{G}}; \hat{\mathbf{U}}, \mathbf{D}_2 \hat{\mathbf{V}}, \hat{\mathbf{W}}]\|_F^2 \\ &+ \lambda_3 \|\mathcal{Y}_3 - [\hat{\mathcal{G}}; \hat{\mathbf{U}}, \hat{\mathbf{V}}, \mathbf{D}_3 \hat{\mathbf{W}}]\|_F^2 \\ &+ \mu \|[\hat{\mathcal{G}}; \hat{\mathbf{U}}, \hat{\mathbf{V}}, \hat{\mathbf{W}}]\|^2. \end{aligned} \quad (6)$$

### C. Proposed algorithm

Rather than finding a local minimum of (6), we propose hereafter a closed-form algorithm as a sub-optimal solution for (5). This new approach is summarized in Algorithm 1, that we will further refer to as isometRic Image Reconstruction by COupled Tensor Tucker Approximation (RICOTTA).

---

#### Algorithm 1: RICOTTA

**input** :  $\mathcal{Y}_1 \in \mathbb{R}^{I_1 \times J \times K}$ ,  $\mathcal{Y}_2 \in \mathbb{R}^{I \times J_2 \times K}$ ,  $\mathcal{Y}_3 \in \mathbb{R}^{I \times J \times K_3}$ ,  
 $\mathbf{D}_1, \mathbf{D}_2, \mathbf{D}_3; R_1, R_2, R_3$   
**output**:  $\hat{\mathcal{Y}} \in \mathbb{R}^{I \times J \times K}$   
1.  $\mathbf{U} \leftarrow \text{tSVD}_{R_1} \left( \begin{bmatrix} \mathbf{Y}_2^{(1)} & \mathbf{Y}_3^{(1)} \end{bmatrix} \right)$ ,  
 $\mathbf{V} \leftarrow \text{tSVD}_{R_2} \left( \begin{bmatrix} \mathbf{Y}_1^{(2)} & \mathbf{Y}_3^{(2)} \end{bmatrix} \right)$ ,  
 $\mathbf{W} \leftarrow \text{tSVD}_{R_3} \left( \begin{bmatrix} \mathbf{Y}_1^{(3)} & \mathbf{Y}_2^{(3)} \end{bmatrix} \right)$   
2.  $\hat{\mathcal{G}} \leftarrow \underset{\mathcal{G}}{\text{argmin}} f_T(\mathcal{G}, \hat{\mathbf{U}}, \hat{\mathbf{V}}, \hat{\mathbf{W}})$ ;  
3.  $\hat{\mathcal{Z}} = [\hat{\mathcal{G}}; \hat{\mathbf{U}}, \hat{\mathbf{V}}, \hat{\mathbf{W}}]$ .

---

Step 1 of RICOTTA estimates the matrix factors  $\mathbf{U}$ ,  $\mathbf{V}$ ,  $\mathbf{W}$  by computing the truncated SVD (tSVD) of the concatenated unfoldings to ranks  $R_1$ ,  $R_2$ ,  $R_3$ , respectively. Step 2 of RICOTTA consists in solving the least-squares problem

$$\underset{\hat{\mathcal{G}}}{\text{arg min}} \|\mathbf{X} \text{vec}\{\hat{\mathcal{G}}\} - \mathbf{z}\|_F^2 + \mu \|\text{vec}\{\hat{\mathcal{G}}\}\|_F^2, \quad (7)$$

with

$$\underbrace{\begin{bmatrix} \sqrt{\lambda_1} \hat{\mathbf{W}} \boxtimes \hat{\mathbf{V}} \boxtimes \mathbf{D}_1 \hat{\mathbf{U}} \\ \sqrt{\lambda_2} \hat{\mathbf{W}} \boxtimes \mathbf{D}_2 \hat{\mathbf{V}} \boxtimes \hat{\mathbf{U}} \\ \sqrt{\lambda_3} \mathbf{D}_3 \hat{\mathbf{W}} \boxtimes \hat{\mathbf{V}} \boxtimes \hat{\mathbf{U}} \end{bmatrix}}_{\mathbf{X}} \text{vec}\{\hat{\mathcal{G}}\} = \underbrace{\begin{bmatrix} \sqrt{\lambda_1} \text{vec}\{\mathcal{Y}_1\} \\ \sqrt{\lambda_2} \text{vec}\{\mathcal{Y}_2\} \\ \sqrt{\lambda_3} \text{vec}\{\mathcal{Y}_3\} \end{bmatrix}}_{\mathbf{z}}. \quad (8)$$

It can be solved through normal equations of the form

$$(\mathbf{X}^T \mathbf{X} + \mu \mathbf{I}) \text{vec}\{\hat{\mathcal{G}}\} = \mathbf{X}^T \text{vec}\{\mathbf{z}\}. \quad (9)$$

The matrix on the left-hand side of (9) is

$$\begin{aligned} \mathbf{X}^T \mathbf{X} &= \mathbf{I}_{R_2 R_3} \boxtimes \lambda_1 \left( \hat{\mathbf{U}}^T \mathbf{D}_1^T \mathbf{D}_1 \hat{\mathbf{U}} \right) \\ &+ \mathbf{I}_{R_3} \boxtimes \lambda_2 \left( \hat{\mathbf{V}}^T \mathbf{D}_2^T \mathbf{D}_2 \hat{\mathbf{V}} \right) \boxtimes \mathbf{I}_{R_1} + \lambda_3 \left( \hat{\mathbf{W}}^T \mathbf{D}_3^T \mathbf{D}_3 \hat{\mathbf{W}} \right) \boxtimes \mathbf{I}_{R_1 R_2}, \end{aligned} \quad (10)$$

and the vector on the right-hand side is

$$\begin{aligned} \mathbf{X}^T \mathbf{z} &= \lambda_1 \text{vec}\{[\mathcal{Y}_1; \hat{\mathbf{U}}^T \mathbf{D}_1^T, \hat{\mathbf{V}}^T, \hat{\mathbf{W}}^T]\} \\ &+ \lambda_2 \text{vec}\{[\mathcal{Y}_2; \hat{\mathbf{U}}^T, \hat{\mathbf{V}}^T \mathbf{D}_2^T, \hat{\mathbf{W}}^T]\} \\ &+ \lambda_3 \text{vec}\{[\mathcal{Y}_3; \hat{\mathbf{U}}^T, \hat{\mathbf{V}}^T, \hat{\mathbf{W}}^T \mathbf{D}_3^T]\}. \end{aligned} \quad (11)$$

Hence (9) can be viewed as a generalized Sylvester equation and efficient solvers can be used. See Appendix A for more details. Therefore, the total computational complexity of RICOTTA is

- $\mathcal{O}((R_1 + R_2 + R_3)IJK)$  flops for the truncated SVDs;
- $\mathcal{O}(\min(R_3^3 + (R_1 R_2)^3; R_1^3 + (R_2 R_3)^3))$  flops for solving the Sylvester equation in Step 2.

### III. EXACT RECOVERY ANALYSIS

In this section, we provide some guarantees for exact recovery of the HRII tensor in the noiseless case. We show that, even though the Tucker decomposition is not unique, it is still possible to achieve exact recovery in the Tucker model. The following theorems and their proofs are inspired by the results of [16, Section V] for tensor reconstruction in remote sensing. However, the model in [16] considered observations which had two degraded dimensions. Hence the recovery conditions that we introduce in this paper allow for a more flexible choice of the ranks.

#### A. Deterministic recovery

Let us start with some deterministic results.

**Theorem III.1.** *Let a Tucker decomposition of  $\mathcal{Z}$  be as in (4). We also assume that  $\mathcal{E}_i$  ( $i = 1, 2, 3$ ) in (2).*

1) *If*

$$\begin{aligned} \text{rank} \left( \begin{bmatrix} \mathbf{Y}_2^{(1)} & \mathbf{Y}_3^{(1)} \end{bmatrix} \right) &= R_1, \quad \text{rank} \left( \begin{bmatrix} \mathbf{Y}_1^{(2)} & \mathbf{Y}_3^{(2)} \end{bmatrix} \right) = R_2, \\ \text{rank} \left( \begin{bmatrix} \mathbf{Y}_1^{(3)} & \mathbf{Y}_2^{(3)} \end{bmatrix} \right) &= R_3, \end{aligned} \quad (12)$$

and either i)  $\text{rank}(\mathbf{D}_1 \mathbf{U}) = R_1$  or ii)  $\text{rank}(\mathbf{D}_2 \mathbf{V}) = R_2$  or iii)  $\text{rank}(\mathbf{D}_3 \mathbf{W}) = R_3$ ,

then there exists only one  $\hat{\mathcal{Z}}$  with multilinear ranks at most  $(R_1, R_2, R_3)$  such that  $\hat{\mathcal{Z}} \bullet_1 \mathbf{D}_1 = \mathcal{Y}_1$ ,  $\hat{\mathcal{Z}} \bullet_2 \mathbf{D}_2 = \mathcal{Y}_2$  and  $\hat{\mathcal{Z}} \bullet_3 \mathbf{D}_3 = \mathcal{Y}_3$ .

2) *If neither conditions i), ii) and iii) hold, then there exists infinitely many  $\hat{\mathcal{Z}}$  of the form (4) satisfying  $\hat{\mathcal{Z}} \bullet_1 \mathbf{D}_1 = \mathcal{Y}_1$ ,  $\hat{\mathcal{Z}} \bullet_2 \mathbf{D}_2 = \mathcal{Y}_2$  and  $\hat{\mathcal{Z}} \bullet_3 \mathbf{D}_3 = \mathcal{Y}_3$ , and  $\|\mathcal{Z} - \hat{\mathcal{Z}}\|_F^2$  can be arbitrary large.*

*Proof.* First, by [25, Theorem 13.16], let us note that the singular values of the matrix  $\mathbf{X}^T \mathbf{X} = \mathbf{I}_{R_3} \boxtimes \mathbf{A} + \mathbf{B} \boxtimes \mathbf{I}_{R_1 R_2}$  in (10) are all sums of the pairs of eigenvalues of the matrices

$$\mathbf{A} = \mathbf{I}_{R_2} \boxtimes \lambda_1 \left( \hat{\mathbf{U}}^T \mathbf{D}_1^T \mathbf{D}_1 \hat{\mathbf{U}} \right) + \lambda_2 \left( \hat{\mathbf{V}}^T \mathbf{D}_2^T \mathbf{D}_2 \hat{\mathbf{V}} \right) \boxtimes \mathbf{I}_{R_1}, \quad (13)$$

$$\mathbf{B} = \lambda_3 \left( \hat{\mathbf{W}}^T \mathbf{D}_3^T \mathbf{D}_3 \hat{\mathbf{W}} \right). \quad (14)$$

We also assume without loss of generality that  $\mathbf{U}$ ,  $\mathbf{V}$ ,  $\mathbf{W}$  have orthonormal columns.

- *Proof of 2)* Assume that  $\text{rank}(\mathbf{D}_1 \mathbf{U}) < R_1$ ,  $\text{rank}(\mathbf{D}_2 \mathbf{V}) < R_2$  and  $\text{rank}(\mathbf{D}_3 \mathbf{W}) < R_3$ . If we set  $\hat{\mathbf{U}} = \mathbf{U}$ ,  $\hat{\mathbf{V}} = \mathbf{V}$ ,  $\hat{\mathbf{W}} = \mathbf{W}$ , then  $\text{rank}(\mathbf{A}) < R_1 R_2$  (by [25]),  $\text{rank}(\mathbf{B}) < R_3$  and  $\text{rank}(\mathbf{X}^T \mathbf{X}) < R_1 R_2 R_3$ .

Therefore (9) is underdetermined and there is an infinite number of solutions  $\widehat{\mathcal{G}} \in \mathbb{R}^{R_1 \times R_2 \times R_3}$ . Note that if we define  $\widehat{\mathcal{Z}} = \llbracket \widehat{\mathcal{G}}; \widehat{\mathbf{U}}, \widehat{\mathbf{V}}, \widehat{\mathbf{W}} \rrbracket$ , then it is an admissible solution, i.e.,  $\widehat{\mathcal{Z}} \bullet_1 \mathbf{D}_1 = \mathcal{Y}_1$ ,  $\widehat{\mathcal{Z}} \bullet_2 \mathbf{D}_2 = \mathcal{Y}_2$  and  $\widehat{\mathcal{Z}} \bullet_3 \mathbf{D}_3 = \mathcal{Y}_3$ . Due to the orthogonality of the bases,  $\|\mathcal{Z} - \widehat{\mathcal{Z}}\|_F^2 = \|\mathcal{G} - \widehat{\mathcal{G}}\|_F^2$  which can be arbitrary large due to the non-uniqueness of the solution to (9).

- *Proof of 1)* Let us choose  $\widehat{\mathbf{U}} \in \mathbb{R}^{I \times R_1}$ ,  $\widehat{\mathbf{V}} \in \mathbb{R}^{J \times R_2}$ ,  $\widehat{\mathbf{W}} \in \mathbb{R}^{K \times R_3}$  to be orthogonal bases of the row spaces of  $\begin{bmatrix} \mathbf{Y}_2^{(1)} & \mathbf{Y}_3^{(1)} \end{bmatrix}$ ,  $\begin{bmatrix} \mathbf{Y}_1^{(2)} & \mathbf{Y}_3^{(2)} \end{bmatrix}$  and  $\begin{bmatrix} \mathbf{Y}_1^{(3)} & \mathbf{Y}_2^{(3)} \end{bmatrix}$ , respectively. By (12), the ranks of the unfoldings do not drop after degradation, hence

$$\widehat{\mathbf{U}} = \mathbf{U}\mathbf{Q}_U, \quad \widehat{\mathbf{V}} = \mathbf{V}\mathbf{Q}_V, \quad \widehat{\mathbf{W}} = \mathbf{W}\mathbf{Q}_W,$$

where  $\mathbf{Q}_U$ ,  $\mathbf{Q}_V$ ,  $\mathbf{Q}_W$  are rotation matrices. Due to the conditions on the ranks of  $\mathbf{D}_1\mathbf{U}$ ,  $\mathbf{D}_2\mathbf{V}$ ,  $\mathbf{D}_3\mathbf{W}$ , we get that  $\text{rank}(\mathbf{X}^T\mathbf{X}) = R_1R_2R_3$  because of (13)–(14). Hence there exists a unique solution  $\widehat{\mathcal{G}}$  to (9). Finally, we note that the reconstructed tensor can be written as

$$\text{vec}\{\widehat{\mathcal{Z}}\} = (\widehat{\mathbf{W}} \otimes \widehat{\mathbf{V}} \otimes \widehat{\mathbf{U}}) (\mathbf{X}^T\mathbf{X} + \mu\mathbf{I})^{-1} \mathbf{X}^T \mathbf{z},$$

and does not depend on the rotation matrices  $\mathbf{Q}_U$ ,  $\mathbf{Q}_V$ ,  $\mathbf{Q}_W$  due to the definition of  $\mathbf{X}$ . Hence the reconstructed tensor  $\widehat{\mathcal{Z}}$  is unique.  $\square$

### B. Generic recovery

**Theorem III.2.** Assume that  $\mathbf{D}_1 \in \mathbb{R}^{I_1 \times I}$ ,  $\mathbf{D}_2 \in \mathbb{R}^{J_2 \times J}$ , and  $\mathbf{D}_3 \in \mathbb{R}^{K_3 \times K}$  are fixed full row-rank matrices. Let

$$\mathcal{Z} = \llbracket \mathcal{G}; \mathbf{U}, \mathbf{V}, \mathbf{W} \rrbracket, \quad (15)$$

where  $\mathcal{G} \in \mathbb{R}^{R_1 \times R_2 \times R_3}$ ,  $R_1 \leq I$ ,  $R_2 \leq J$ ,  $R_3 \leq K$ , and  $\mathbf{U} \in \mathbb{R}^{I \times R_1}$ ,  $\mathbf{V} \in \mathbb{R}^{J \times R_2}$ ,  $\mathbf{W} \in \mathbb{R}^{K \times R_3}$  are random tensor and matrices, distributed according to an absolutely continuous probability distribution. We also assume that  $\mathcal{E}_i$  ( $i = 1, 2, 3$ ) in (2).

1. If either  $R_3 \leq K_3$  or  $R_1 \leq I_1$  or  $R_2 \leq J_2$ , and

$$\begin{cases} R_1 \leq \min(R_3, K_3)R_2, \\ R_2 \leq \min(R_3, K_3)R_1 \\ R_3 \leq \min(R_1, I_1) \min(R_2, J_2), \end{cases} \quad (16)$$

then with probability 1 there exists a unique tensor  $\widehat{\mathcal{Z}}$  such that  $\widehat{\mathcal{Z}} \bullet_1 \mathbf{D}_1 = \mathcal{Y}_1$ ,  $\widehat{\mathcal{Z}} \bullet_2 \mathbf{D}_2 = \mathcal{Y}_2$  and  $\widehat{\mathcal{Z}} \bullet_3 \mathbf{D}_3 = \mathcal{Y}_3$ .

2. If  $(R_1, R_2, R_3) > (I_1, J_2, K_3)$ , then the reconstruction is non-unique, i.e. there exist an continuum of  $\widehat{\mathcal{Z}}$  such that  $\widehat{\mathcal{Z}} \bullet_1 \mathbf{D}_1 = \mathcal{Y}_1$ ,  $\widehat{\mathcal{Z}} \bullet_2 \mathbf{D}_2 = \mathcal{Y}_2$  and  $\widehat{\mathcal{Z}} \bullet_3 \mathbf{D}_3 = \mathcal{Y}_3$ ; in fact,  $\|\widehat{\mathcal{Z}} - \mathcal{Z}\|$  can be arbitrary large.

*Proof.* • *Proof of 2)* follows from Theorem III.1, part 2).

- *Proof of 1)* Without loss of generality, we can replace  $\mathbf{D}_1$ ,  $\mathbf{D}_2$ ,  $\mathbf{D}_3$  with the following matrices of same size:

$$\mathbf{D}_1 = \begin{bmatrix} \mathbf{I}_{I_1} \\ \mathbf{0} \end{bmatrix}^T, \quad \mathbf{D}_2 = \begin{bmatrix} \mathbf{I}_{J_2} \\ \mathbf{0} \end{bmatrix}^T, \quad \mathbf{D}_3 = \begin{bmatrix} \mathbf{I}_{K_3} \\ \mathbf{0} \end{bmatrix}^T.$$

Let us explain why it is so for  $\mathbf{D}_1 \in \mathbb{R}^{I_1 \times I}$ . There exists a non-singular matrix  $\mathbf{T}$  such that  $\mathbf{D}_1\mathbf{T} = [\mathbf{I}_{I_1} \ \mathbf{0}]$ . If we take  $\widetilde{\mathbf{U}} = \mathbf{T}^{-1}\mathbf{U}$  then  $\mathbf{D}_1\mathbf{U} = \mathbf{D}_1\widetilde{\mathbf{U}}$ . Note that a nonsingular transformation preserves absolute continuity

of the distribution; hence  $\mathbf{U}$  has an absolutely continuous distribution if and only if  $\widetilde{\mathbf{U}}$  has one.

Therefore under the assumptions on distributions of  $\mathbf{U}$ ,  $\mathbf{V}$ ,  $\mathbf{W}$ , the following hold with probability 1:

$$\begin{aligned} R_1 \leq I_1 &\Rightarrow \text{rank}(\mathbf{U}_{1:I_1,:}) = R_1, \\ R_2 \leq J_2 &\Rightarrow \text{rank}(\mathbf{V}_{1:J_2,:}) = R_2, \\ R_3 \leq K_3 &\Rightarrow \text{rank}(\mathbf{W}_{1:K_3,:}) = R_3. \end{aligned}$$

Next, we will show how the other set of conditions imply (12). We will only prove it for the first condition, and the others are analogous. Note that we can write

$$\begin{aligned} \mathbf{Y}_2^{(1)} &= (\mathbf{W} \otimes \mathbf{V}_{1:J_2,:}) \mathbf{G}^{(2)} \mathbf{U}^T, \\ \mathbf{Y}_3^{(1)} &= (\mathbf{W}_{1:K_3,:} \otimes \mathbf{V}) \mathbf{G}^{(2)} \mathbf{U}^T, \end{aligned}$$

which are at most rank  $R_1$ . Due to the semicontinuity of the rank function,  $\begin{bmatrix} \mathbf{Y}_2^{(1)} & \mathbf{Y}_3^{(1)} \end{bmatrix}$  will be generically of rank  $R_1$  if we can provide just a simple example of  $\mathbf{U}$ ,  $\mathbf{V}$ ,  $\mathbf{W}$ ,  $\mathcal{G}$  achieving the condition  $\text{rank}\left(\begin{bmatrix} \mathbf{Y}_2^{(1)} & \mathbf{Y}_3^{(1)} \end{bmatrix}\right) = R_1$ . This is analogous to finding an example of such  $\mathbf{U}$ ,  $\mathbf{V}$ ,  $\mathbf{W}$ ,  $\mathcal{G}$  achieving the conditions  $\text{rank}(\mathbf{Y}_2^{(1)}) = R_1$  and  $\text{rank}(\mathbf{Y}_3^{(1)}) = R_1$ . Indeed, if  $R_1 \leq \min(R_2, J_2)R_3$  and since  $R_3 \leq K_3$ , such an example is given by

$$\mathbf{U} = \begin{bmatrix} \mathbf{I}_{R_1} \\ \mathbf{0} \end{bmatrix}, \quad \mathbf{V} = \begin{bmatrix} \mathbf{I}_{R_3} \\ \mathbf{0} \end{bmatrix}, \quad \mathbf{W} = \begin{bmatrix} \mathbf{I}_{R_3} \\ \mathbf{0} \end{bmatrix}, \quad \mathbf{G}^{(1)} = \begin{bmatrix} \mathbf{I}_{R_1} \\ \mathbf{0} \end{bmatrix},$$

hence the proof is complete.  $\square$

In Figure 1, we illustrate the statement of Theorem III.2. The region (a) where the HRII is recoverable is pictured in green while the red region (b) corresponds to ranks for which the HRII is not recoverable exactly. The hatched area corresponds to cases in which the conditions (16) are not satisfied. Figure 1 indicates that one can pick two given multilinear ranks possibly as large as the dimensions of the image, as long as the third one remains small. As a comparison, the theorems in [16] required both  $R_1$  and  $R_2$  to be small in order to increase  $R_3$ , which is more restrictive.

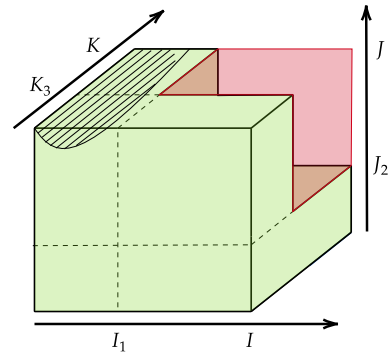


Fig. 1. Identifiability region depending on  $R_1$ ,  $R_2$  and  $R_3$ .

#### IV. EXPERIMENTS

All simulations were run on a MacBook Pro with 2.3 GHz Intel Core i5 and 16GB RAM. The code was implemented in MATLAB. For basic tensor operations we used TensorLab 3.0 [26]. A software reproducing our experiments is available online at [https://github.com/cprevost4/RICOTTA\\_Software](https://github.com/cprevost4/RICOTTA_Software).

##### A. Setup and validation

We compared the reconstruction performance of RICOTTA to two state-of-the-art reconstruction procedures [9]. The super-resolution (SR) algorithm combines the three LRIs into one single HRII. Compared to the previously published work, here a preprocessing step was applied in order to cast the acquired data and observation model into the separable form given in Eq. 2. This consisted of a resampling, as in the native image space, degradation occurs in the third dimension (called slice direction). In the general case, native MRI scans may not be strictly orthogonal (often they are manually adjusted by the radiographer to the anatomy), so a rigid transformation (3D rotation and translation) is applied to the 3D image. This is achieved by an image interpolation from the native voxel coordinates (available in the standard medical image format, DICOM) to the target set of orthogonal coordinates. In case the scans are already orthogonal, this reduces to a simple permutation of the dimensions. Two SR algorithms were considered. The first one used Tikhonov regularization and will be referred to as SR-T. The second one used feature-preserving Beltrami regularization [27] and will be further denoted to as SR-B. The hyperparameters for these methods were tuned according to the original work [9].

To evaluate the quality of the reconstructed images  $\hat{\mathcal{Z}}$ , we considered two quantitative metrics [28]. The first one was the peak signal to noise ratio (PSNR), defined as

$$\text{PSNR} = \frac{10}{K} \sum_{k=1}^K \log_{10} \left( \frac{IJE \{(\mathcal{Z})_{:::,k}\}}{\|(\mathcal{Z})_{:::,k} - (\hat{\mathcal{Z}})_{:::,k}\|_F^2} \right), \quad (17)$$

where  $E\{\cdot\}$  denoted the expectation operator. The PSNR should be as large as possible.

The second metric was the Cross-Correlation (CC), taking values between 0 and 1:

$$\text{CC} = \frac{1}{IJK} \left( \sum_{k=1}^K \rho(\mathcal{Z}_{:::,k}, \hat{\mathcal{Z}}_{:::,k}) \right), \quad (18)$$

where  $\rho(\cdot, \cdot)$  is the Pearson correlation coefficient between the estimated and original slices.

Additionally, we considered the sharpness index (SI) [29] that is widely used for automatic image restoration and image quality assessment. We computed the average SI across the two first spatial dimensions ( $\text{SI}_{1,2}$ ) and the average SI across the frontal slice dimension ( $\text{SI}_3$ ). The reconstruction methods should maximize the SI. We also showed the computational time for each algorithm, given by the `tic` and `toc` functions of MATLAB. These metrics will be displayed in the following tables. The best results will be shown in bold case.

##### B. Data description

We assessed the performance of our approach on a set of synthetic and real datasets. The first real dataset was a physical phantom. The second one was a whole brain dataset for which a healthy volunteer underwent a cerebral MRI.

1) *Phantom data*: A test object (physical phantom), used for quality control and resolution assessment, was scanned with a 3T Prisma MRI scanner (Siemens Healthineers, Erlangen, Germany). First, a high-resolution image was obtained and was used as the ground truth for comparison of the different SR reconstruction methods. The acquisition used a turbo spin echo sequence, with a native resolution of  $1 \times 1 \times 1.1 \text{ mm}^3$  (1.1 mm was the finest resolution allowed by the scanner here), which was interpolated to  $1 \times 1 \times 1 \text{ mm}^3$  and zero-padded in the third dimension to produce a reference tensor  $\mathcal{Z} \in \mathbb{R}^{224 \times 224 \times 224}$ , considered as the ground truth image (HRII). The scan time for HRII was 6 min 30 s.

To assess the performance of RICOTTA in a controlled environment, a synthetic dataset was generated from the ground truth data (HRII). The low-resolution observations were artificially computed from a degradation matrix  $\mathbf{D} \in \mathbb{R}^{56 \times 224}$  so that the downsampling ratio was  $d = 4$ . White Gaussian noise was added to the observations to generate 25dB SNR.

Then we acquired actual low resolution scans of the phantom in three orthogonal orientations (LRI data). Firstly, the brain LRI data were acquired with voxels of size  $1 \times 1 \times 4 \text{ mm}^3$  in each of the three orientations. The three observations were such that  $\mathcal{Y}_1 \in \mathbb{R}^{56 \times 224 \times 224}$ ,  $\mathcal{Y}_2 \in \mathbb{R}^{224 \times 56 \times 224}$  and  $\mathcal{Y}_3 \in \mathbb{R}^{224 \times 224 \times 56}$ , respectively. Thus the downsampling ratio between the HRII and the LRI was  $d = 4$ . The degradation matrices  $\mathbf{D}_1$ ,  $\mathbf{D}_2$ ,  $\mathbf{D}_3$  were selection-and-averaging matrices. The imaging system was tuned such that  $\mathbf{D}_1 = \mathbf{D}_2 = \mathbf{D}_3 \in \mathbb{R}^{56 \times 224}$ . The acquisition of each LRI took approximately 2 min.

Secondly, the brain LRI data were acquired with voxels of size  $1 \times 1 \times 8 \text{ mm}^3$ . The downsampling ratio between the HRII and the LRI was  $d = 8$ , yielding  $\mathbf{D}_1 = \mathbf{D}_2 = \mathbf{D}_3 \in \mathbb{R}^{28 \times 224}$ . The acquisition of each of the three LRI in that case took approximately 1 min.

2) *Real brain data*: The volunteer experiment was conducted on a 3T Signa HDxt MRI scanner (General Electric, Milwaukee, USA). The volunteer study was approved by an ethics committee and written informed consent was obtained (ClinicalTrials.gov identifier: NCT02887053).

Similar to the phantom experiment, we acquired a high-resolution reference dataset of the whole brain (HRII). The acquisition used a fast gradient echo sequence with a native resolution of  $1 \times 1 \times 1 \text{ mm}^3$  which was zero-padded in the third dimension to produce a reference tensor  $\mathcal{Z} \in \mathbb{R}^{224 \times 224 \times 224}$ , considered as the ground truth image (HRII). The scan time for HRII was 8 min. Brain LRI data were obtained with voxels of size  $1 \times 1 \times 4 \text{ mm}^3$  (downsampling ratio of 4). The acquisition of each LRI took approximately 2 min.

Finally an additional LRI dataset was acquired, to push the scanner resolution limit, with voxel of size  $0.5 \times 0.5 \times 2 \text{ mm}^3$  (total scan time was 11.5 min). Here the 3 volumes were placed such that their intersection covered the cerebellum region, and the SR reconstruction aimed at  $0.5 \times 0.5 \times 0.5 \text{ mm}^3$ , which is significantly below the typical resolution of clinical brain scans on a 3T scanner.

##### C. Parameter selection

In this subsection, we investigated the impact on the regularization parameter  $\mu$  and the balance parameters  $\lambda_i$  ( $i = 1, 2, 3$ ) on the reconstruction performance. For each dataset, we computed the reconstruction metrics as a function

of several values of the parameters. For the physical phantom dataset with  $d = 4$ , we chose  $R = (220, 220, 50)$ . For the dataset with  $d = 8$ , we chose  $R = (220, 220, 30)$ . We chose the ranks as large as possible in the plane axes, which forced  $R_3$  to be rather small. More experiments on the choice of the ranks are to be investigated in future works.

We proceeded as follows. First, we fixed  $\lambda_i = 1$ , ( $i = 1, 2, 3$ ) and ran RICOTTA for  $\mu \in \{1 \cdot 10^{-4}, 2 \cdot 10^{-4}, 2 \cdot 10^{-4}, \dots, 1, 2, 5\}$ . Then, we selected the value of  $\mu$  that yielded the best reconstruction metrics. We ran RICOTTA for  $\lambda_1 = \lambda_2$  and  $\lambda_3$  taking values in  $\{0.1, 0.2, 0.3, \dots, 1\}$ . The results were displayed on Figures 2 to 5. Similarly, we took the values of  $\lambda_i$  yielding the best reconstruction metrics.

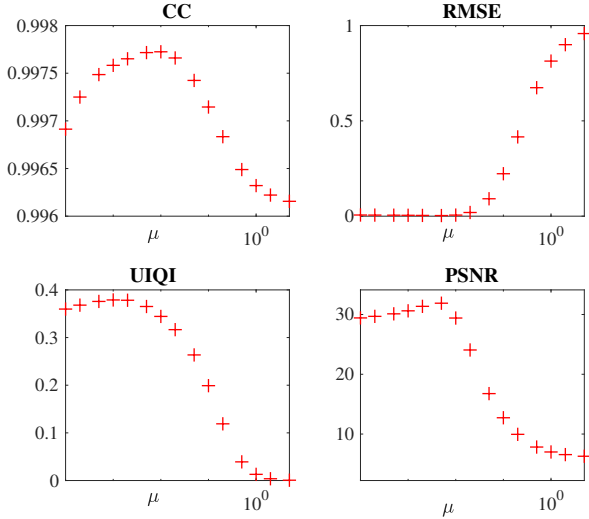


Fig. 2. Reconstruction metrics as a function of  $\mu$  for physical phantom dataset ( $d = 4$ ).

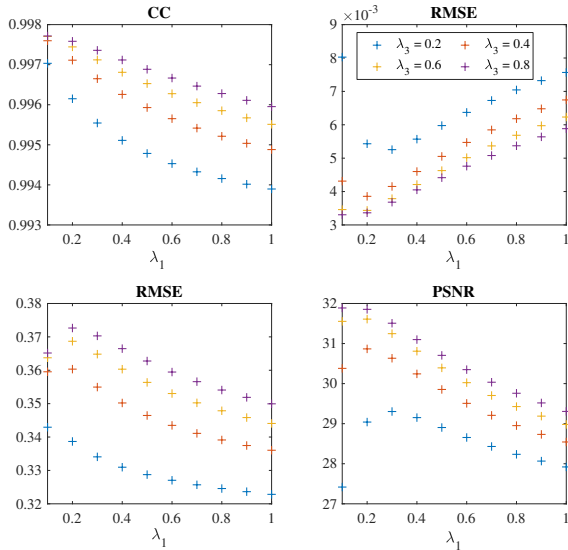


Fig. 3. Reconstruction metrics as a function of  $\lambda_1$  and  $\lambda_3$  physical phantom dataset ( $d = 4$ ).

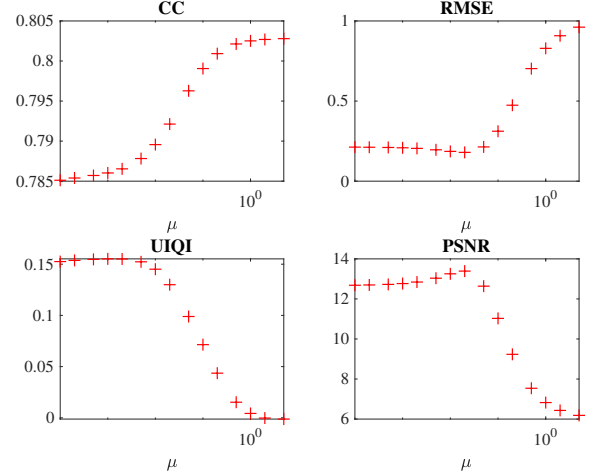


Fig. 4. Reconstruction metrics as a function of  $\mu$  for quality test phantom ( $d = 8$ ).

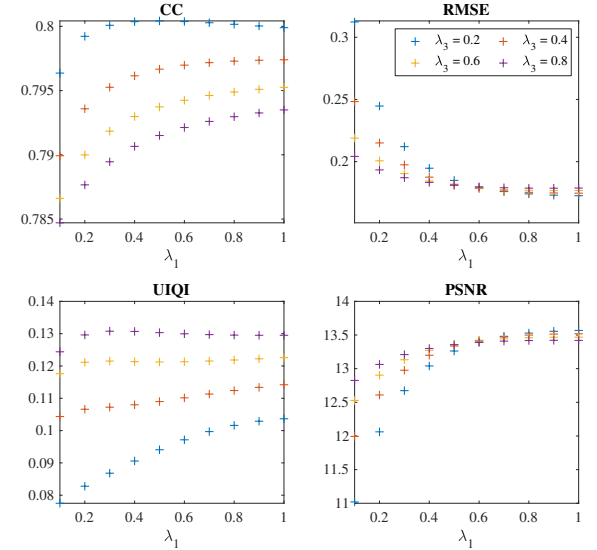


Fig. 5. Reconstruction metrics as a function of  $\lambda_1$  and  $\lambda_3$  quality test phantom ( $d = 8$ ).

#### D. Performance for image reconstruction

We assessed the performance of RICOTTA for image reconstruction using a quality test phantom acquisition.

1) *Synthetic data (no noise).*: We ran RICOTTA with multilinear ranks  $R = (220, 220, 50)$  and weights  $\lambda_1 = \lambda_2 = 0.2$  and  $\lambda_3 = 0.8$ . We set the value of the regularization parameter  $\mu = 0.005$ . The reconstruction metrics were available in Table I. Slices of the original and reconstructed images along the three acquisition axes were displayed in Figure 6.

Alg.	PSNR	CC	SI <sub>1,2</sub>	SI <sub>3</sub>	Time (s)
RICOTTA	29.7842	0.99644	<b>87.4662</b>	<b>508.6188</b>	<b>239.5144</b>
SR-T	18.0585	0.9911	72.9317	381.5021	252.0798
SR-B	<b>40.4194</b>	<b>0.99964</b>	81.9257	451.1445	402.446

TABLE I

RECONSTRUCTION FOR SYNTHETIC DATASET (NO NOISE).

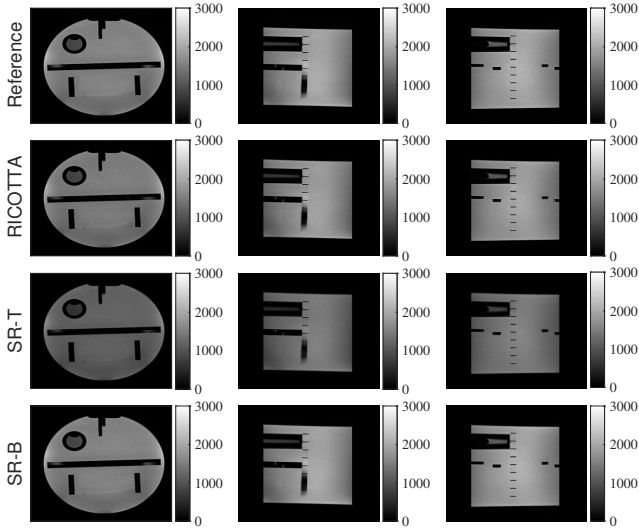


Fig. 6. Original and reconstructed slices of the HRII for synthetic dataset (no noise).

Although SR-B gave the best PSNR and CC, RICOTTA yielded the highest sharpness indices and lowest computation time.

2) *Synthetic data (noisy).*: We ran RICOTTA with multilinear ranks  $R = (220, 220, 50)$  and weights  $\lambda_1 = \lambda_2 = 0.2$  and  $\lambda_3 = 0.8$ . We set the value of the regularization parameter  $\mu = 0.005$ . The reconstruction metrics were available in Table II. Slices of the original and reconstructed images along the three acquisition axes were displayed in Figure 7.

Alg.	PSNR	CC	SI <sub>1,2</sub>	SI <sub>3</sub>	Time (s)
RICOTTA	29.4486	0.99588	<b>85.9152</b>	<b>445.3585</b>	<b>200.1546</b>
SR-T	17.9778	<b>0.99691</b>	34.2228	199.0813	266.9506
SR-B	<b>29.896</b>	0.99543	33.2338	210.6509	707.259

TABLE II  
RECONSTRUCTION FOR SYNTHETIC DATASET (NOISY).

RICOTTA yielded the highest sharpness indices and lowest computation time, and its PSNR and CC were comparable to those of SR-B and SR-T, respectively.

3) *Physical phantom with  $d = 4$ .*: We ran RICOTTA with multilinear ranks  $R = (220, 220, 50)$  and weights  $\lambda_1 = \lambda_2 = 0.2$  and  $\lambda_3 = 0.8$ . We set the value of the regularization parameter  $\mu = 0.005$ . The reconstruction metrics were available in Table III. Slices of the original and reconstructed images along the three acquisition axes were displayed in Figure 8.

Alg.	PSNR	CC	SI <sub>1,2</sub>	SI <sub>3</sub>	Time (s)
RICOTTA	18.5317	0.96311	<b>104.4038</b>	<b>528.2747</b>	215.2314
SR-T	<b>19.3865</b>	<b>0.96383</b>	87.4277	330.5614	<b>49.0915</b>
SR-B	17.1011	0.96135	103.31	424.8156	219.7359

TABLE III  
RECONSTRUCTION FOR QUALITY TEST PHANTOM ( $d = 4$ ).

The proposed approach provided slightly lower reconstruction metrics than SR-T, but had the best sharpness indices. The computation time of RICOTTA was comparable to that of SR-B, but had better reconstruction performance. The reconstructed image displays accurately the details along the three axes.

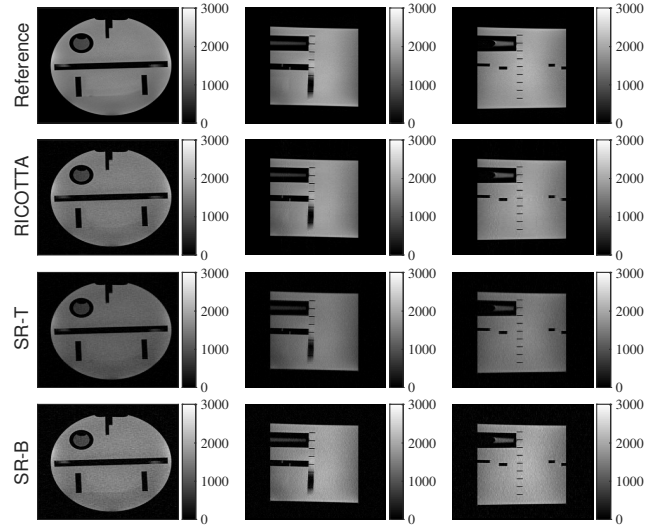


Fig. 7. Original and reconstructed slices of the HRII for synthetic dataset (noisy).

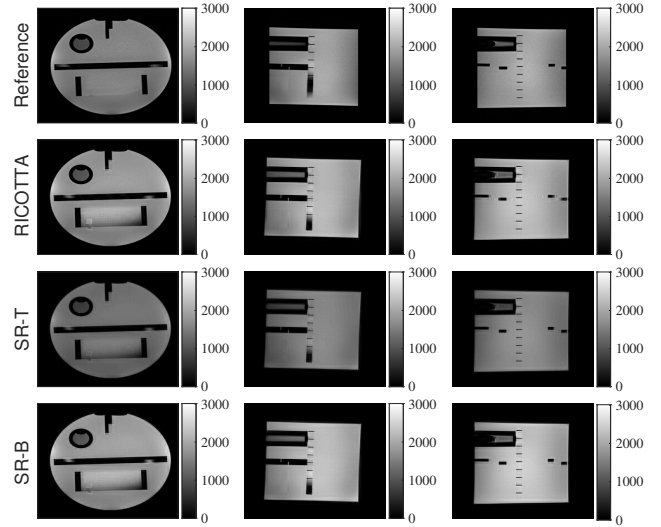


Fig. 8. Original and reconstructed slices of the HRII for quality test phantom ( $d = 4$ ).

4) *Physical phantom with  $d = 8$ .*: We ran RICOTTA with multilinear ranks  $R = (220, 220, 30)$  and weights  $\lambda_1 = \lambda_2 = 1$  and  $\lambda_3 = 0.8$ . We set the value of the regularization parameter  $\mu = 0.02$ . The reconstruction metrics were available in Table IV and slices of the original and reconstructed images were displayed in Figure 9.

Alg.	PSNR	CC	SI <sub>1,2</sub>	SI <sub>3</sub>	Time (s)
RICOTTA	<b>20.9511</b>	<b>0.96332</b>	80.2722	<b>429.7209</b>	<b>11.9669</b>
SR-T	18.0914	0.96257	84.2081	329.2856	15.3575
SR-B	19.8084	0.96137	95.8012	397.4636	219.3982

TABLE IV  
RECONSTRUCTION FOR QUALITY TEST PHANTOM ( $d = 8$ ).

RICOTTA yielded better PSNR, CC and SI in the frontal dimension compared to the SR-reconstruction method, but slightly lower SI in the plane dimensions. It had the lowest

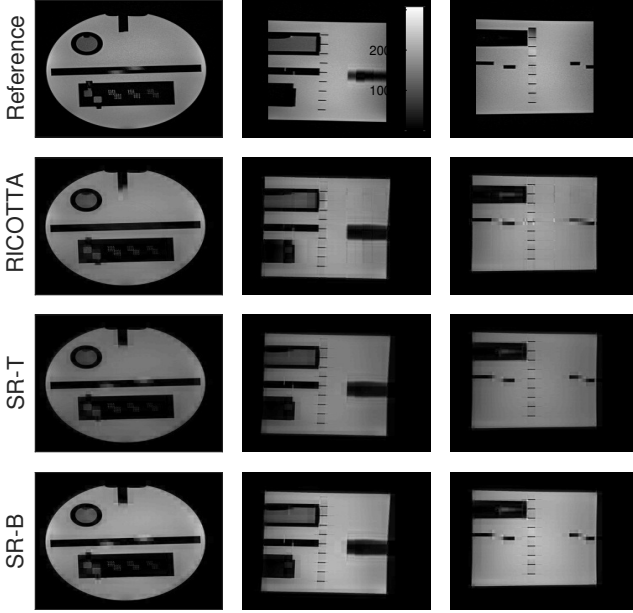


Fig. 9. Original and reconstructed slices of the HRII for quality test phantom ( $d = 8$ ).

computation time for our implementation. The visual quality of the reconstruction was similar to that of SR-T and SR-B.

5) *Reconstruction for brain scans (Brain1)*: We ran RICOTTA with multilinear ranks  $R = (220, 220, 50)$  and weights  $\lambda_1 = \lambda_2 = 0.2$  and  $\lambda_3 = 0.8$ . We set the value of the regularization parameter  $\mu = 0.001$ . The results were available in Table V and in Figure 10.

Alg.	PSNR	CC	SI <sub>1,2</sub>	SI <sub>3</sub>	Time (s)
RICOTTA	<b>24.7645</b>	<b>0.91535</b>	174.3469	<b>580.9331</b>	<b>236.5069</b>
SR-T	22.5571	0.88549	<b>278.0689</b>	422.8249	266.2802
SR-B	22.7096	0.88426	264.0003	447.6295	361.3989

TABLE V

RECONSTRUCTION FOR BRAIN DATASET ( $d = 4$ ).

The proposed algorithm provided better PSNR and CC than the state-of-the-art. In particular, the SI in the frontal dimension was way higher than that provided by the SR algorithms. RICOTTA had the lowest computation time. However, the sharpness index in the two first dimensions was the lowest.

For this dataset, the reconstruction time was comparable to the acquisition time of the reference HRII. However, performing reconstruction rather than full acquisition has the advantage of reducing possible artifacts due to patient motion. Furthermore, the computation time of RICOTTA could be further reduced by considering a block-wise approach.

6) *Reconstruction for brain scans (Brain2)*: We ran RICOTTA with multilinear ranks  $R = (90, 90, 20)$  and weights  $\lambda_1 = \lambda_2 = 0.1$  and  $\lambda_3 = 1$ . We set the value of the regularization parameter  $\mu = 0.005$ . Due to the sensor's physical limitations, no reference was available for this dataset. The sharpness indices and computation time were available in Table VI. Slices of the reconstructed images were displayed in Figure 11.

RICOTTA provided the best SI in the third dimension and lowest computation time. Its SI in the plane directions was

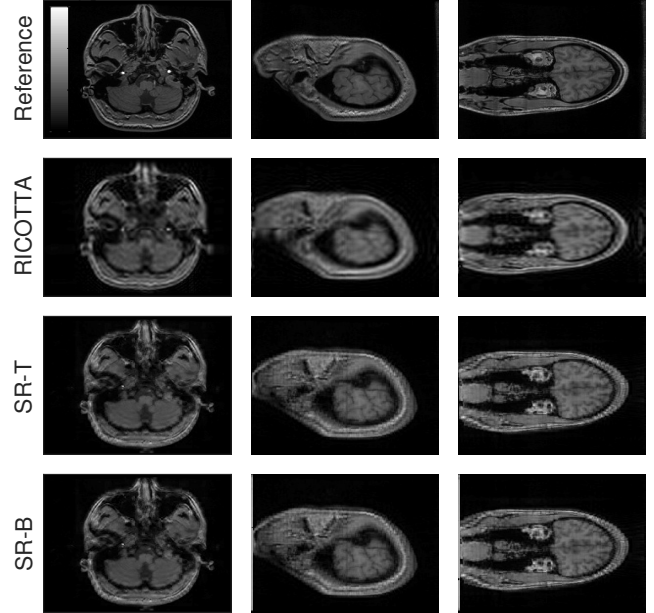


Fig. 10. Original and reconstructed slices of the HRII for real brain data ( $d = 4$ ).

Alg.	SI <sub>1,2</sub>	SI <sub>3</sub>	Time (s)
RICOTTA	9.1968	<b>30.1341</b>	<b>1.0286</b>
SR-T	<b>17.1788</b>	11.3023	1.3088
SR-B	9.1231	11.6167	7.0642

TABLE VI

RECONSTRUCTION FOR BRAIN DATASET ( $d = 5$ ).

comparable to that of SR-B.

## V. CONCLUSION

In this paper, we proposed a novel tensor method for reconstructing MRI high-resolution 3D volumes. The proposed algorithm achieves exact reconstruction for a variety of multilinear ranks. Our simulations on synthetic and real data shows

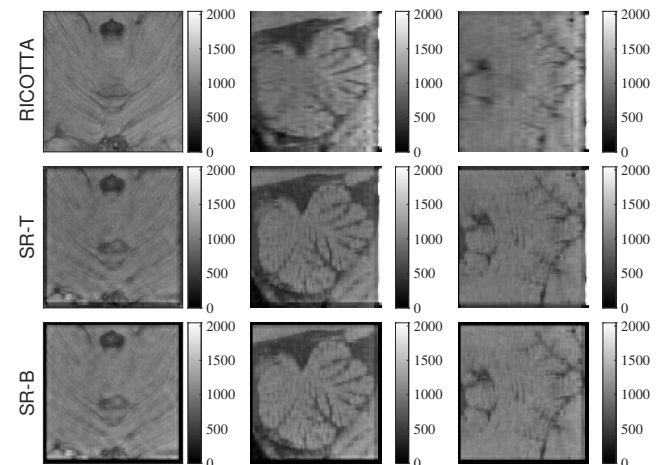


Fig. 11. Original and reconstructed slices of the HRII for real brain data (cervlet).

that RICOTTA performs good reconstruction with a competitive time. We hope that this work opens new perspectives on using tensor factorization in medical imaging applications. The proposed method should be applicable to a wide range of MRI acquisition techniques, *e.g.*,  $T_1$ -weighted,  $T_2$ -weighted, or diffusion-weighted imaging in the brain, heart or other organs. It could help improve the trade-off between scan time, resolution, SNR and contrast in MRI. Still several questions remain open, such as the choice of the model parameters, including the multilinear ranks. Different regularization operators can be envisioned, such as Beltrami regularization, as considered in [9]. It is also possible to envision an algorithm capable to account for (possibly non-orthogonal) rotation operators between the observations and the HR1. This matter is of great interest and will be investigated in future works.

#### APPENDIX

Equation (9) can be seen as a generalized Sylvester equation of the form

$$\mathbf{A}\widehat{\mathbf{G}}\mathbf{B} + \mathbf{C}\widehat{\mathbf{G}}\mathbf{D} = \mathbf{E}, \quad (19)$$

where  $\mathbf{G}$  is an unfolding of  $\widehat{\mathbf{G}}$ .

We propose two options for converting (9) into (19). In the first case,  $\widehat{\mathbf{G}} = \mathbf{g}^{(1)\top} \in \mathbb{R}^{R_1 \times R_2 \times R_3}$ ,

$$\mathbf{A} = \lambda_1 (\mathbf{U}^\top \mathbf{D}_1^\top \mathbf{D}_1 \mathbf{U}), \quad \mathbf{B} = \mathbf{I}_{R_2 R_3}, \quad \mathbf{C} = \mathbf{I}_{R_1}, \\ \mathbf{D} = \lambda_2 (\mathbf{V}^\top \mathbf{D}_2^\top \mathbf{D}_2 \mathbf{V}) + \lambda_3 (\mathbf{W}^\top \mathbf{D}_3^\top \mathbf{D}_3 \mathbf{W}),$$

and  $\mathbf{E} \in \mathbb{R}^{R_2 R_3 \times R_1}$  is a matricization of  $\mathbf{X}^\top \mathbf{z}$ .

In the second case,  $\widehat{\mathbf{G}} = \mathbf{g}^{(3)} \in \mathbb{R}^{R_1 R_2 \times R_3}$ ,

$$\mathbf{A} = \lambda_1 (\mathbf{U}^\top \mathbf{D}_1^\top \mathbf{D}_1 \mathbf{U}) + \lambda_2 (\mathbf{V}^\top \mathbf{D}_2^\top \mathbf{D}_2 \mathbf{V}), \\ \mathbf{B} = \mathbf{I}_{R_3}, \quad \mathbf{C} = \mathbf{I}_{R_1 R_2}, \quad \mathbf{D} = \lambda_3 (\mathbf{W}^\top \mathbf{D}_3^\top \mathbf{D}_3 \mathbf{W}),$$

and  $\mathbf{E} \in \mathbb{R}^{R_1 R_2 \times R_3}$  is a matricization of  $\mathbf{X}^\top \mathbf{z}$ .

The two options are equivalent and the fastest one is chosen according to the multilinear rank. The complexity for solving the generalized Sylvester equation (19) is thus  $O(m^3 + n^3)$  flops for  $\widehat{\mathbf{G}} \in \mathbb{R}^{m \times n}$  if fast solvers, such as Hessenberg-Schur or Bartels-Stewart methods [30], [31], [32], are used.

#### REFERENCES

- [1] Esben Plenge, Dirk H. J. Poot, Monique Bernsen, Gyula Kotek, Gavin Houston, Piotr Wielopolski, Louise van der Weerd, Wiro J. Niessen, and Erik Meijering, "Super-resolution methods in MRI: Can they improve the trade-off between resolution, signal-to-noise ratio, and acquisition time?," *Magnetic Resonance in Medicine*, vol. 68, no. 6, pp. 1983–1993, 2012.
- [2] Eric Van Reeth, Ivan W. K. Tham, Cher Heng Tan, and Chueh Loo Poh, "Super-resolution in magnetic resonance imaging: A review," *Concepts in Magnetic Resonance Part A*, vol. 40A, no. 6, pp. 306–325, 2012.
- [3] M. Delbany, A. Bustin, J. Poujol, I. Thomassin-Naggara, J. Felblinger, P.-A. Vuissoz, and F. Odille, "One-millimeter isotropic breast diffusion-weighted imaging: Evaluation of a superresolution strategy in terms of signal-to-noise ratio, sharpness and apparent diffusion coefficient," *Magnetic Resonance in Medicine*, vol. 81, no. 4, 2019.
- [4] Ozan Oktay, Wenjia Bai, Matthew Lee, Ricardo Guerrero, Konstantinos Kamnitsas, Jose Caballero, Antonio de Marvao, Stuart Cook, Declan O'Regan, and Daniel Rueckert, "Multi-input Cardiac Image Super-Resolution Using Convolutional Neural Networks," in *Medical Image Computing and Computer-Assisted Intervention - MICCAI 2016*, Sebastien Ourselin, Leo Joskowicz, Mert R. Sabuncu, Gozde Unal, and William Wells, Eds., Cham, 2016, Lecture Notes in Computer Science, pp. 246–254, Springer International Publishing.
- [5] Jun Shi, Zheng Li, Shihui Ying, Chaofeng Wang, Qingping Liu, Qi Zhang, and Pingkun Yan, "MR Image Super-Resolution via Wide Residual Networks With Fixed Skip Connection," *IEEE Journal of Biomedical and Health Informatics*, vol. 23, no. 3, pp. 1129–1140, May 2019.
- [6] Dana Lahat, Tülay Adalı, and Christian Jutten, "Multimodal data fusion: an overview of methods, challenges, and prospects," *Proceedings of the IEEE*, vol. 103, no. 9, pp. 1449–1477, 2015.
- [7] A. Gholipour, J.A. Estroff, and S.K. Warfield, "Robust Super-Resolution Volume Reconstruction From Slice Acquisitions: Application to Fetal Brain MRI," *IEEE Transactions on Medical Imaging*, vol. 29, no. 10, pp. 1739–1758, Oct. 2010.
- [8] H Greenspan, G Oz, N Kiryati, and S Peled, "MRI inter-slice reconstruction using super-resolution," *MAGNETIC RESONANCE IMAGING*, vol. 20, no. 5, pp. 437–446, June 2002.
- [9] F. Odille, A. Bustin, B. Chen, P.-A. Vuissoz, and J. Felblinger, "Motion-corrected, super-resolution reconstruction for high-resolution 3d cardiac cine mri," in *International Conference on Medical Image Computing and Computer-Assisted Intervention*. Springer, 2015, pp. 435–442.
- [10] F Rousseau, O Glenn, and C Studholme, *A novel approach to high resolution fetal brain MR imaging*, vol. 3749 of *Lecture Notes in Computer Science*, Springer, Berlin New York London [etc.], 2005.
- [11] Xin Zhang, Edmund Y. Lam, Ed X. Wu, and Kenneth K. Y. Wong, "Application of Tikhonov Regularization to Super-Resolution Reconstruction of Brain MRI Images," in *Medical Imaging and Informatics*, Xiaohong Gao, Henning Müller, Martin J. Loomes, Richard Comley, and Shuqiang Luo, Eds., number 4987 in *Lecture Notes in Computer Science*, pp. 51–56. Springer Berlin Heidelberg, 2008.
- [12] Sébastien Tourbier, Xavier Bresson, Patric Hagmann, Jean-Philippe Thiran, Reto Meuli, and Meritxell Bach Cuadra, "Efficient total variation algorithm for fetal brain MRI reconstruction," *Medical image computing and computer-assisted intervention: MICCAI ... International Conference on Medical Image Computing and Computer-Assisted Intervention*, vol. 17, no. Pt 2, pp. 252–259, 2014.
- [13] Feng Shi, Jian Cheng, Li Wang, Pew-Thian Yap, and Dinggang Shen, "LRTV: MR Image Super-Resolution with Low-Rank and Total Variation Regularizations," *IEEE transactions on medical imaging*, vol. 34, no. 12, pp. 2459–2466, Dec. 2015.
- [14] Aurelien Bustin, Damien Voilliot, Anne Menini, Jacques Felblinger, Christian de Chillou, Darius Burschka, Laurent Bonnemains, and Freddy Odille, "Isotropic Reconstruction of MR Images Using 3D Patch-Based Self-Similarity Learning," *IEEE transactions on medical imaging*, vol. 37, no. 8, pp. 1932–1942, Aug. 2018.
- [15] C. I. Kanatsoulis, X. Fu, N. D. Sidiropoulos, and W.-K. Ma, "Hyperspectral Super-Resolution: A Coupled Tensor Factorization Approach," *IEEE Trans. Signal Process.*, vol. 66, no. 24, pp. 6503–6517, 2018.
- [16] C. Prévost, K. Usevich, P. Comon, and D. Brie, "Hyperspectral Super-Resolution with Coupled Tucker Approximation: Identifiability and SVD-based algorithms," *IEEE Trans. Signal Process.*, vol. 68, pp. 931–946, 2020.
- [17] G. Zhang, X. Fu, J. Wang, X.-L. Zhao, and M. Hong, "Spectrum cartography via coupled block-term tensor decomposition," *IEEE Trans. Signal Process.*, 2020.
- [18] B. Yaman, S. Weingärtner, N. Kargas, N. D. Sidiropoulos, and M. Akçakaya, "Low-rank tensor models for improved multidimensional mri: Application to dynamic cardiac  $t_1$  mapping," *IEEE transactions on computational imaging*, vol. 6, pp. 194–207, 2019.
- [19] C. I. Kanatsoulis, X. Fu, N. D. Sidiropoulos, and M. Akçakaya, "Tensor Completion from Regular Sub-Nyquist Samples," *arXiv e-prints*, p. arXiv:1903.00435, Mar. 2019.
- [20] N. Yokoya, C. Grohnfeldt, and J. Chanussot, "Hyperspectral and multispectral data fusion: A comparative review of the recent literature," *IEEE Trans. Geosci. Remote Sens.*, vol. 5, no. 2, pp. 29–56, 2017.
- [21] L. De Lathauwer, "Decompositions of a Higher-Order Tensor in Block Terms—Part II: Definitions and Uniqueness," *SIAM J. Matrix Anal. Appl.*, vol. 30, no. 3, pp. 1033–1066, 2008.
- [22] P. Comon, "Tensors: A brief introduction," *IEEE Signal Process. Mag.*, vol. 31, no. 3, pp. 44–53, 2014.
- [23] T. G. Kolda and B. W. Bader, "Tensor Decompositions and Applications," *SIAM Review*, vol. 51, no. 3, pp. 455–500, 2009.
- [24] G. H. Golub, P. C. Hansen, and D. P. O'Leary, "Tikhonov regularization and total least squares," *SIAM journal on matrix analysis and applications*, vol. 21, no. 1, pp. 185–194, 1999.
- [25] A. J. Laub, *Matrix analysis for scientists and engineers*, vol. 91, Siam, 2005.
- [26] N. Vervliet, O. Debals, L. Sorber, M. Van Barel, and L. De Lathauwer, *Tensorlab 3.0*, Available online, 2016.
- [27] D. Zosso and A. Bustin, "A primal-dual projected gradient algorithm for efficient beltrami regularization," *Computer Vision and Image Understanding*, pp. 14–52, 2014.
- [28] W. Pei, G. Wang, and X. Yu, "Performance evaluation of different references based image fusion quality metrics for quality assessment of remote sensing image fusion," in *2012 IEEE International Geoscience and Remote Sensing Symposium*. IEEE, 2012, pp. 2280–2283.
- [29] G. Blanchet and L. Moisan, "An explicit sharpness index related to global phase coherence," in *2012 IEEE International Conference on*

- Acoustics, Speech and Signal Processing (ICASSP)*. IEEE, 2012, pp. 1065–1068.
- [30] R. H. Bartels and G. W. Stewart, “Solution of the matrix equation  $AX+XB=C$ ,” *Communications of the ACM*, vol. 15, no. 9, pp. 820–826, 1972.
- [31] G. Golub, S. Nash, and C. Van Loan, “A Hessenberg-Schur method for the problem  $AX+XB=C$ ,” *IEEE Trans. Autom. Control*, vol. 24, no. 6, pp. 909–913, 1979.
- [32] V. Simoncini, “Computational methods for linear matrix equations,” *SIAM Review*, vol. 58, no. 3, pp. 377–441, 2016.